

## Fast Temperature and True Airspeed Measurements with the Airborne Ultrasonic Anemometer–Thermometer (AUSAT)

D. CRUETTE, A. MARILLIER, J. L. DUFRESNE, AND J. Y. GRANDPEIX

*Laboratoire de Météorologie Dynamique, CNRS, Université Pierre et Marie Curie, Paris, France*

P. NACASS AND H. BELLEC

*Météo France, CNRM, Centre d'Aviation Météorologique, Bretigny-sur-Orge, France*

(Manuscript received 8 December 1998, in final form 14 October 1999)

### ABSTRACT

An airborne thermometer–anemometer with fast response is designed and built using the well-known sonic anemometer–thermometer technique. The shape of this new airborne sonic sensor, without the conventional style probes, is a cylinder with its axis colinear to the aircraft's longitudinal axis. The true airspeed and the air temperature are measured in the same volume. A previous paper described a preliminary version of this sensor and presented data of flight tests obtained on board Météo France's Cessna 206. This new paper shows an improved sensor and the results obtained on faster aircraft such as the CNRS–INSU's Fokker 27 and the Météo France's Merlin IV. First, the sensor and the principle of the measuring method are described, then data collected during several flights from 1996 to 1998 are presented. Although this new thermometer–anemometer is not completely calibrated, it provides mean data very close of those measured by conventional sensors but with a response time 30 times shorter.

### 1. Introduction

A fast-response thermometer for the measurement of static air temperature on board a research aircraft is required for numerous purposes including the study of temperature spectra, turbulent heat flux, and calculations of true airspeed.

Most temperature measurements from an aircraft are based on the immersion of a sensing element in the airflow. The local static temperature of the air is obtained after correction of compressional heating, probe housing distortion, and evaporative cooling associated with wetting within the clouds. Moreover, if the sensing element is a thin wire, it must be protected against impacts of droplets, insects, sand grains, etc. Then, the effect of the flow distortions is difficult to evaluate.

Sonic techniques were first applied to airborne temperature measurements in the 1960s. However, these attempts failed due to difficulties in designing the sensor housing and to low capacities of airborne electronics and computers.

During the past decade, patient efforts have been

made at the Université de Paris (Université Pierre et Marie Curie/Laboratoire de Météorologie Dynamique du CNRS) for the development of the Airborne Ultrasonic Anemometer Thermometer (AUSAT) (Marillier et al. 1991). The objective of this sensor is to directly measure both the aircraft's true airspeed and the fast fluctuations of the air temperature.

Our early airborne prototypes used triaxial sensor geometry with style probes as ground-based sensors. However, style vibrations and interference between transducers required to channel the airflow into a cylinder so as to be unidirectional.

Flight tests began with a slow motorglider aircraft (airspeed <80 kt), followed by the light Morane-Saulnier 893 and the Cessna 206 aircraft (125 to 135 kt), then by faster instrumented research aircrafts such as the Fokker 27 (180 kt) and finally the Merlin IV (220 kt at 2800 ft of altitude).

Since May 1996, the AUSAT is mounted on Météo France's Merlin IV to be compared with other airborne thermometers and has flown more than 200 h. First, it was mounted on a pole above the fuselage (Fig. 1), but too far (5.70 m) from the other fast sensors gathered around the front radome. So, at the beginning of 1997, the AUSAT was mounted on one of the standard pylon under the aircraft's nose (Fig. 2) with an angle of 4° down in respect to the fuselage axis; therefore, the angle of attack is near 0 for a flight leg at 100 m s<sup>-1</sup>. It was

---

*Corresponding author address:* Dr. Philippe Nacass, Météo France/CNRM/CAM, Aérodrome du CEV, Bâtiment AMOR, F-91228 Brétigny-sur-Orge, France.  
E-mail: philippe.nacass@meteo.fr



FIG. 1. Photograph of the AUSAT mounted above the fuselage of the Merlin IV in 1996.

in test for four international field experiments in Livourne (Italy, 1996), Canary Islands (ACE 2, 1997), above the Mediterranean Sea (FETCH, 1998), and France (TRAC, 1998).

Data recorded during the last flights, after improvements of the sensor's shape, electronics, and location on the aircraft, suggest that AUSAT is capable of measuring at a high rate the true airspeed and fast air temperature fluctuations. The main advantages of this instrument are the following:

- true airspeed is directly measured from the transit times of two emitter–receiver paths,
- air temperature is intrinsically measured since the velocity of the sound depends only upon this state parameter (first-order accuracy),
- the very short transit time of the sonic wave (less than 0.7 ms) allows a measurement rate up to  $10^3$  Hz and therefore a large bandwidth, and
- the absence of psychrometric effect due to evaporation of droplets trapped by the sensing element as it occurs for impact thermometers.

## 2. Description of the sensor

A sonic sensor mounted on an aircraft cannot have the same shape as a ground-based sensor, essentially



FIG. 2. Photograph of the AUSAT mounted under the fuselage of the Merlin IV after 1997.

TABLE 1. Dimensions and weight of the AUSAT sensor.

Overall length	620 mm
Outer diameter	220 mm
Inner diameter	150 mm
Channel length	212 mm
Weight	15 kg

because of a fast permanent airflow around it. Consequently, the shape of the AUSAT sensor is a 0.63-m-long open pipe with a 0.21-m outer diameter and a 0.15-m inner diameter (Table 1 and Fig. 3). It weighs 15 kg. The body is made of aluminium Au4G, the leading and trailing edges are manufactured in polypropylen blocks; thus, the occurrence of wetting and icing is reduced.

These characteristics are comparable to the standard canister designed for most of the microphysic probes which is a 0.79-m-long cylinder with a 0.18-m diameter and a weight of 17 kg. Therefore, the AUSAT may be mounted on an aircraft using one of the standard pylon suited for the microphysic probes manufactured, for example, by Particle Measuring Systems (PMS).

The measuring principle of the AUSAT is based on the determination of two transit times. As for all intervallometry technics, a long path is preferable. This partly explains the sensor's dimensions.

Two pairs of sonic emitter–receiver transducers (E1–R1 and E2–R2, Fig. 4) are situated in two diametral and orthogonal planes of a cuboid directed by the cylinder axis. This new setting is to prevent interferences between the two acoustic paths. In order to avoid their direct immersion in the airflow, these four transducers are settled into the sensor wall. They are made of cylindrical piezoelectric ceramic with a resonance frequency of 120 kHz. To limit the interference between the unpaired transducers, emitters have a narrow radiation field.

## 3. Principle of measurement

### a. Basic principle

The method is a classical one (Suomi and Businger, 1959) and has already been successfully used for

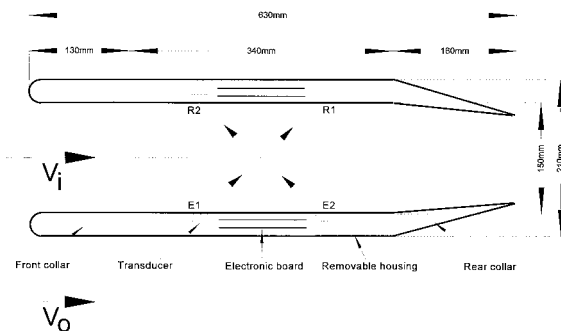


FIG. 3. Cross section of the axisymmetric body of the AUSAT with the front and rear collars, the emitters E1 and E2, the receivers R1 and R2, and the main dimensions.

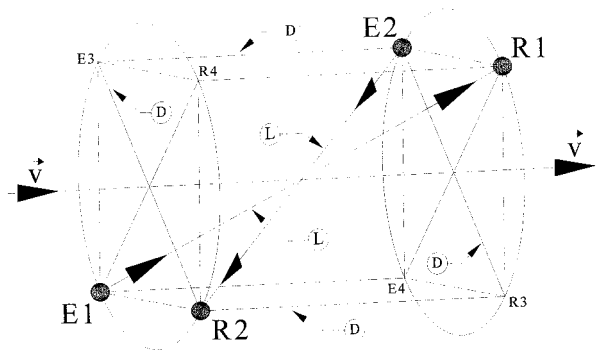


FIG. 4. Schematic view of the signal paths in the volume of measurement.

ground-based instruments (Mitsuta 1966). Each sonic source emits a short pulse of compression–dilatation waves that propagate with a phase velocity  $c$  relative to the air. The characteristics of these waves can be derived from the general sound propagation theory, where sound “rays” in an elastic medium are defined as lines drawn normally to the propagating wave front (appendix Aa).

This concept allows a fairly good description of the sound wave field, that may be considered as spherical at a distance from the source greater than 10 wavelengths.

After that, the transducer setting in the measurement volume gives a very easy set of equations (appendix Ab) to determine the following:

- the sound velocity  $c$  (m s<sup>-1</sup>),

$$c = \frac{L}{\sqrt{2}} \left( \frac{1}{t_1^2} + \frac{1}{t_2^2} \right)^{1/2}, \quad (1)$$

- the relative wind speed  $V$  (m s<sup>-1</sup>),

$$V = \frac{L}{\sqrt{2}} \left( \frac{1}{t_1} - \frac{1}{t_2} \right), \quad (2)$$

- and the temperature of the dry air  $T$  (K),

$$T = \frac{L^2}{2\gamma_a R_a} \left( \frac{1}{t_1^2} + \frac{1}{t_2^2} \right). \quad (3)$$

In these above equations,  $L$  is the distance between E1–R1 and E2–R2;  $\gamma_a = c_{pa}/c_{va}$ , the ratio of specific heats (J kg<sup>-1</sup> K<sup>-1</sup>) at constant pressure  $c_{pa}$  and at constant volume  $c_{va}$  of dry air; and  $R_a = R^*/M_a$ , is the specific constant of dry air with  $R^*$  (J K<sup>-1</sup>) the universal gas constant and  $M_a$  (kg), the molecular weight of dry air.

#### b. Rear convergent and speed correction

Wind tunnel tests have shown that the faster the airspeed is, the greater is the signal attenuation. Due to the sensor’s cylindrical shape, a conical convergent base

is set at the rear exhaust part for slowing down the flow in the measurement volume.

If the upstream velocity out of the cylinder is noted  $V_o$  and if the velocity in one point in the measurement volume is noted  $V_i$ , then a coefficient  $\mu$  equals to the ratio  $V_i/V_o$  may define the airstream slowing down. Thus, this AUSAT measurement of the velocity can afford an interesting other way to obtain the aircraft’s true air speed  $V_o$ .

Wind tunnel measurements and computational fluid dynamics gave  $\mu$  equal to 0.36 and indicated that it only depends on the sensor’s geometry. This value was found independent of the incident flow angle; the AUSAT was tested with an angle of attack up to 4°. Therefore,

$$V_o = V_i \left( \frac{1}{\mu} \right).$$

#### c. Dynamic heating

But the decrease of velocity leads to an increase of upstream temperature  $T_o$  to the inner temperature  $T_i$ . The overheating  $\Delta T = T_i - T_o$ , and thus the correction to apply to the measured temperature may be calculated by using the thermodynamic relation for compressible flows during an adiabatic process of an ideal gas:

$$T_o + \frac{V_o^2}{2c_{pa}} = T_i + \frac{V_i^2}{2c_{pa}}. \quad (4)$$

The above relation, true for incompressible and compressible flows does not require further compressibility correction. Thus we obtain

$$\Delta T = \frac{V_o^2}{2c_{pa}} (1 - \mu^2) = \frac{V_i^2}{2c_{pa}} \left( \frac{1}{\mu^2} - 1 \right). \quad (5)$$

Since  $V_i$  is measured, this correction only requires to know the value of  $\mu$ . This correction is included in the software and computed in real time.

#### d. Humidity correction

Therefore, the AUSAT is self-containing for the measurement of the aircraft true airspeed  $V_o$  but provides an air temperature  $T_o$  that must be corrected a posteriori by taking into account the air humidity. Note that the aircraft true airspeed as measured by AUSAT does not need this humidity correction.

The temperature  $T_o$  obtained by combining relations (3) and (5) is not the true air temperature. Indeed, the so-calculated temperature is correct for strictly dry air and not for the humid air in the atmosphere because, in this case,  $\gamma$  and  $R$  are both a function of the specific humidity of the air.

The relation between the true temperature  $T'_o$  and the calculated temperature  $T_o$  is

$$T'_o = T_o (1 - 0.518q), \quad (6)$$

where the specific humidity of the air  $q$  is the ratio of the water vapor density  $\rho_v$  ( $\text{kg m}^{-3}$ ) to the humid air density  $\rho_v + \rho_a$  where  $\rho_a$  is the dry air density. This correction has to be made a posteriori, by using simultaneous humidity airborne data collected by a fast hygrometer with the same bandpass and rate of acquisition as the AUSAT.

So, we have for the humidity correction,

$$\Delta T_o = T_o - T'_o = 0.518qT_o.$$

This correction is a linear function of two independent variables, even if  $q$  ( $\text{kg kg}^{-1}$ ) and  $T_o$  (K) are not really independent in the atmosphere. Thus, the magnitude of  $\Delta T_o$  may be calculated for different values of  $q$  and  $T_o$ . For example, if the temperature ranges between 250 and 290 K and the humidity varies between 3 and 7  $\text{g kg}^{-1}$ , the humidity correction is then between  $0.39^\circ$  and  $1.05^\circ\text{C}$ . For the same humidity range, at  $T_o = 270$  K,  $\Delta T_o$  varies from  $0.42^\circ$  to  $0.98^\circ\text{C}$ . It also can be seen that an uncertainty of  $0.1 \text{ g kg}^{-1}$  yields to an error of  $0.015^\circ\text{C}$ .

Note that in formula (5) for the dynamic heating, using  $c_{pa}$  for dry air in place of  $c_p$  for humid air, with  $c_p = c_{pa}(1 + 0.84q)$ , yields to an error on  $T$  smaller than  $0.04^\circ\text{C}$  when  $q$  is less than  $10 \text{ g kg}^{-1}$  and smaller than  $0.07^\circ\text{C}$  for  $q = 20 \text{ g kg}^{-1}$ .

#### 4. Main measurement problems

##### a. Influence of the turbulence

An acoustic wave in a fluid is extremely sensitive to air turbulences, which deform wave fronts in a very chaotic way. So, in air turbulence, received signals show strong amplitude instabilities. Turbulence may also be responsible for phase instabilities of the received signals. Even weak, these perturbations may induce a spurious noise in the high-frequency domain.

These difficulties have been overcome, first by an optimization of the sensor's shape to reduce air turbulence in the vicinity of the transducers, and secondly by using an electronic detection device with low sensitivity to the small amplitude instabilities: transducers are settled into a cavity in the sensor wall so they do not create a barrier to the airflow and then a local turbulence in their vicinity; further, the measurement frequency is at 1024 Hz, near the upper limit imposed by the sensor dimensions. The transit time of the sonic wave along the upwind path is in the order of 1 ms when  $V_o = 100 \text{ m s}^{-1}$ , so the time interval between two measurements cannot be less.

The AUSAT sensor measures the mean velocity of an acoustic pulse in the measuring volume. It may be shown (appendix B) that it constitutes a natural frequency filter and calculations show that for a true airspeed of about  $100 \text{ m s}^{-1}$  (inner speed  $V_i$  about  $40 \text{ m s}^{-1}$ ) frequencies larger than 300 Hz are strongly damped. So, with a frequency measurement of 1024 Hz the Shan-

non's law is complied and moreover, as successive pulses have a comparable amplitude, it is easy to realize a correct detection with a delay line (section 5).

##### b. Refraction of the sound rays

Interface between the airstream and each of the four cavities is provided by a thin grid. In the cavity the air is quiet. Then, when acoustic rays pass through the grid, they are submitted to a sharp wind shear. It can be shown that in such conditions, the sound rays are refracted as light electromagnetic waves through a diopre (Snell's law). An approximate theory (Morse and Ingard 1986) gives a method to calculate the deviation of a sound ray as a function of the wind shear. This phenomenon induces an additional attenuation of the received signal as it has been observed during wind-tunnel tests of AUSAT. For large values of the shear (airspeed near  $120 \text{ m s}^{-1}$ ), the refracted ray may travel along the boundary layer and no energy is transmitted to the receiver.

At this point, the presence of the rear convergent is completely justified. Indeed, turbulence in the pipe and signal attenuation increase quickly with the airspeed. Moreover, symmetry deficiencies in the sensor's geometry due to construction faults involve measurement errors that increase also with the airspeed. Finally, due to the refraction phenomenon, the sensor could not work at the cruise speed of a classical research aircraft without its rear convergent.

#### 5. Brief description of electronics

Emitters and receivers are piezoelectric transducers with a resonance frequency of 120 kHz. Emitters are simultaneously excited by a very short pulse (500 V of amplitude and 1024 Hz of repetition frequency).

As the received signal looks like a wave train (Fig. 5), the arrival time is rather difficult to estimate. Our method consists in choosing a characteristic point on the received signal (e.g., the first zero crossing amplitude of the third cycle). Then, the signal transit time is obtained by adding a constant of calibration to the measured time between the starting pulse and this characteristic point. Thus, the arch of sinusoid is selected as soon as the signal overshoots a definite threshold. A synchronous pip is generated by the first crossing zero amplitude and interrupts a numeric count initiated by the starting pulse.

In electronics, this well-known method (Marillier et al. 1991; Ovarlez et al. 1978) is very accurate even the received signal is noisy because detection occurs when a specified arch of sinusoid crosses the zero axis, that is, at a point where the signal slope is maximal. However, when there are very large turbulent temperature fluctuations that induce strong signal amplitude variations—this method may have a major drawback if the detection threshold has a fixed value: in such conditions, another arch of the sinusoid may be chosen yielding

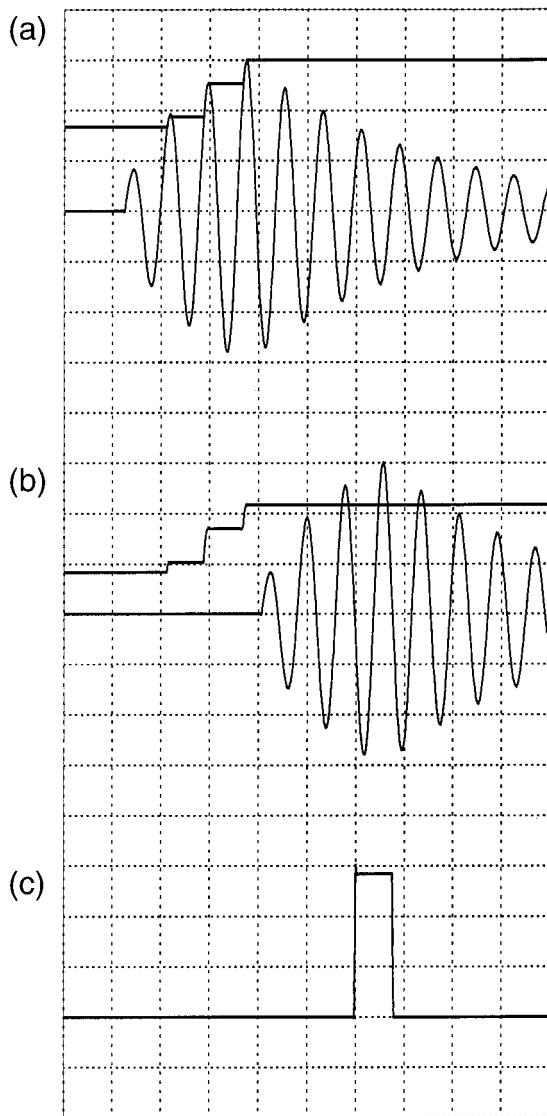


FIG. 5. Oscilloscope displays of signal detection. (a) Received signal and peak detection. (b) Delayed signal and choice of an oscillation peak. (c) Detection of the first zero crossing after the chosen peak. (Time is in  $\mu\text{s}$ .)

to a quantified error on the temperature measurements with a step of  $5^\circ$ , which is unacceptable. To solve this problem the threshold is adjusted at each measurement. For that, the signal maximum amplitude is measured each time (Fig. 5a): the signal is sent in a delay line (Fig. 5b) and each time the detection threshold is automatically adjusted to a fixed proportion of the maximum amplitude of the delayed signal. Therefore, as soon as instabilities are not too strong, the same arch of sinusoid is detected. Of course, the delay induced by electronics is taken into account for transit time determination.

In addition to the previous described functions, an amplitude regulation loop is used for the received signal

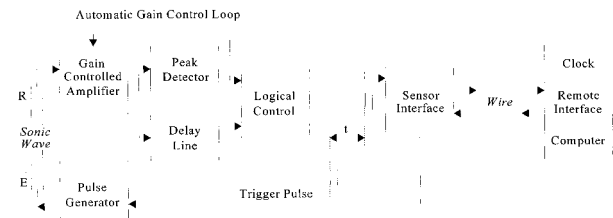


FIG. 6. Block diagram of the electronic unit.

(Fig. 6). The voltage generated by the peak detector is also used for adjusting the sensitiveness of the received signal amplification. Indeed, receivers provide very weak signals that must be absolutely amplified. But, as the received signal amplitude varies with the altitude (atmospheric pressure) and the airspeed of the aircraft, the amplification coefficient must be adjusted. Nevertheless, this kind of feedback control is ineffective against high-frequency atmospheric turbulences that needs the detection device here above described.

For each measurement channel, a numerical count clocked at 48 MHz converts the transit time for delivering to a microcomputer. This clock defines the resolution of the transit time (appendix Ac). This numerical count can be chosen for averaged on eight, four, or two measures. All data presented in this paper are averaged on two measures.

Thus, 512, 256, or 128 data by second may be delivered by each channel and used to calculate, in real time and at the same rate, the "sonic" temperature and the aircraft airspeed. Both digital and analogic output are available.

Air temperature and aircraft airspeed are low pass filtered at 50 Hz before being sent to the airborne acquisition system that samples the signal at 100 or 200 Hz. All data presented in this paper are sampled at 200 Hz.

## 6. Wind tunnel and computational flow modeling

The distortion of airflow streamlines around the aircraft varies during a flight. The cylindrical shape of the sensor straightens the airflow upstream of the measurement volume. Both modeling and wind tunnel studies were employed by ONERA (the French Aerospace Research Agency) to optimize the shape and dimensions of a rear convergent base in order to use the AUSAT on board a middle speed aircraft (up to  $120 \text{ m s}^{-1}$ ).

Recently, a commercial computational fluid dynamics code (Fluent-Rampant) was used at Météo France/CNRM/CAM to determine the velocity decrease of the airflow within the cylinder. A three-dimensional body mesh was constructed as a structured mesh with approximately 75 000 three-dimensional hexahedral cells (220 000 quadrilateral faces) to describe the domain comprising the airflow around and through the AUSAT. The boundary conditions were defined for a velocity

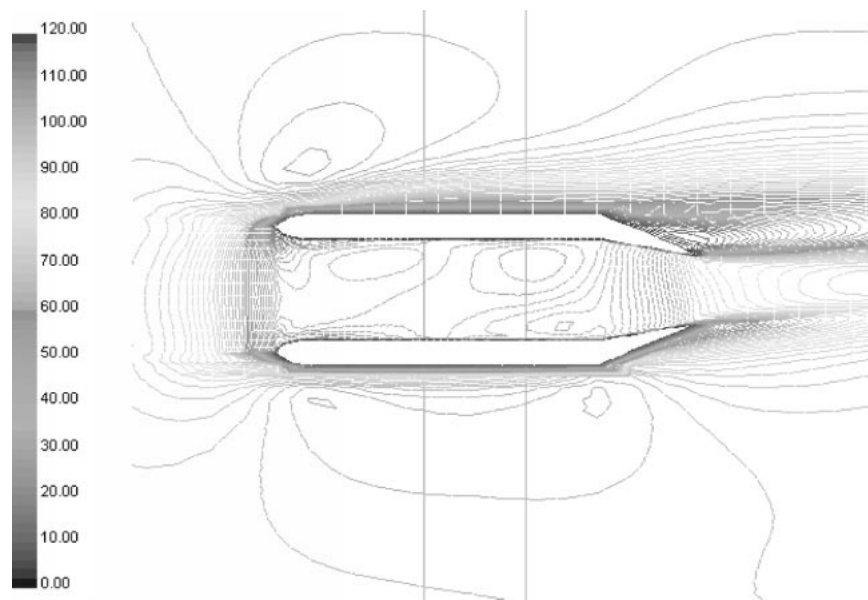


FIG. 7. Contour plot of velocity magnitude predicted by the model on a plane of symmetry for a 3D simulation with a 6° incident angle.

inlet of  $100 \text{ m s}^{-1}$  at a temperature of 300 K. The inlet flow field was initialized with various angles of attack up to  $6^\circ$ .

These values were computed because if the AUSAT is mounted on the pole above the fuselage (Fig. 1), its axis is strictly parallel to the aircraft longitudinal axis; therefore, in a flight leg of measurement (at  $100 \text{ m s}^{-1}$ ), the angle of attack of both aircraft and AUSAT is  $+4^\circ$ . On the contrary, if the AUSAT is mounted on one of pod under the radome (Fig. 2), it is settled, as all sensors around the nose, with an angle of  $-4^\circ$  in relation to the aircraft axis; therefore, in flight at  $100 \text{ m s}^{-1}$ , the AUSAT's angle of attack is near  $0^\circ$ .

Simulations are used to predict the static pressure contours, pressure coefficient  $K_p$  (Nacass 1992), velocity vectors, plots of the velocity in and out of the sensor

volume, and drag coefficient ( $C_d = 0.024$  without a pod). For example, Fig. 7 shows velocity contours of airflow distortion for  $6^\circ$  of angle of attack. And in the measurement volume of the AUSAT, along its longitudinal axis, the predicted velocity is around  $40 \text{ m s}^{-1}$  for an angle of attack of 0 or  $6^\circ$  (Fig. 8).

**7. Sensor characteristics and tested performances**

Electronics characteristics are presented in Table 2. Measurement resolutions given in Table 3 have been determined from the amplitude of the high-frequency noise observed during tests.

Theoretical detection threshold for the AUSAT model presented in this paper (clock at 48 MHz and  $V_o$  at  $100 \text{ m s}^{-1}$ ) is  $0.023^\circ\text{C}$  for the temperature and  $0.007 \text{ m s}^{-1}$  for the true air speed (appendix Ac). With a clock at 100 MHz (electronics in development) it would be possible to obtain  $0.011^\circ\text{C}$  and  $0.003 \text{ m s}^{-1}$ .

**8. Some results**

It must be kept in mind that the AUSAT is still a prototype in test and has not been yet completely and

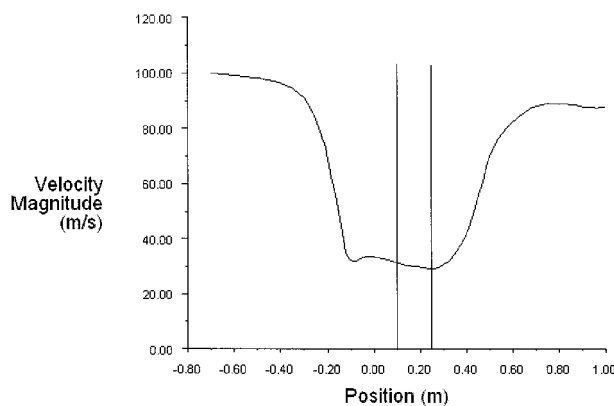


FIG. 8. Predicted velocity magnitude along the centerline of the AUSAT with a  $6^\circ$  incident angle.

TABLE 2. Characteristics of the electronics of the AUSAT signal processing.

Measurement frequency	1024 Hz
Clock frequency	48 MHz
Data integration	Upon 8, 4, or 2 measures, i.e., 128, 256, or 512 data per second
Output filter	Low-pass filter at 50 Hz
Output signal	Analogic and digital (14 bits)

TABLE 3. Measurement parameters of the AUSAT for velocity and temperature.

Airspeed	Tested
Range	0–140 m s <sup>-1</sup>
Resolution	≈0.01 m s <sup>-1</sup> (at 100 m s <sup>-1</sup> )
Digital resolution	0.007 m s <sup>-1</sup> (at 48 MHz)
Bandpass	25–30 Hz
Response time	30 ms
Temperature	
Range	–40° to +30°C
Resolution	≈0.03°C (at 100 m s <sup>-1</sup> )
Digital resolution	0,023°C (at 48 MHz)
Bandpass	25–30 Hz
Response time	30 ms

accurately calibrated. Nevertheless, as seen in this section the AUSAT data are already very close to that obtained from classical airborne sensors.

#### a. General comparison of the time series of three different thermometers

A simple method to compare response time of different thermometers is to obtain their response to a very sharp step of temperature. Such steps are not easy to find in clear air but are usual at the border of cumulus clouds. So, some results obtained during a constant level flight with penetrations in two cumulus turrets during the experience TRAC 98 are presented hereafter.

Figure 9 shows temperature measurements respectively obtained by the AUSAT and by a 102 E4 AL non-deiced Rosemount probe, during a constant-level flight with penetrations into two cumulus cloud turrets. The liquid water content measured by a PMV-100 Gerber probe is also in this figure. This last probe is situated 6.50 m behind the thermometers and data have to be corrected for the time lag approximately equals to 50 ms or 10 data at a rate of 200 Hz taking into account the outer aircraft velocity (100 m s<sup>-1</sup>) and the inner slow down velocity in the AUSAT.

AUSAT temperature presented in this chapter is not calibrated and not linearly corrected to fit the Rosemount temperature in clear air (see section 8c). Thus, data cannot be used for a quantitative comparison but they give a first insight on respective response times.

During penetrations, both thermometers show that the in-cloud air temperature is lower than the surrounding air temperature by about 1.5°C, suggesting an overshooting effect at these levels (in this case, the air temperature in cloud is cooler than out of cloud).

Note the very fast response time of the AUSAT compared to the Rosemount, at the entrance as well as at the exit of the cloud.

On the static pressure record (Fig. 10), we can observe that the aircraft slightly climbed during the first penetration but kept a fairly constant altitude during the second penetration. Consequently, the AUSAT temper-

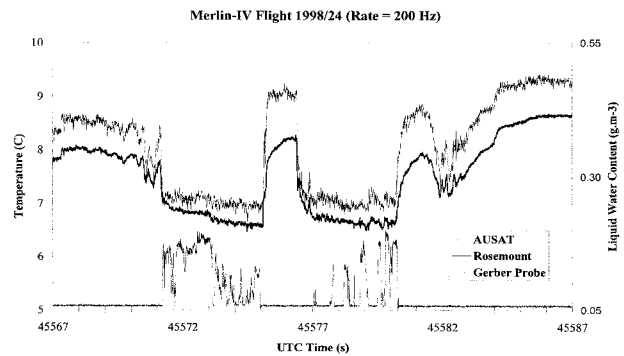


FIG. 9. High rate (200 Hz) time series (20 s) of AUSAT and Rosemount temperatures with the PMV 100 Gerber probe liquid water content.

ature slowly decreases in the first turret and remains fairly constant in the second turret.

During the first cloud turret penetration (lasting 4 s and corresponding to a distance of 400 m), the Gerber probe indicates a more continuous liquid water content than during the second one. The Rosemount record shows a more pronounced temperature decrease than the AUSAT, perhaps due to wetting of the Rosemount housing (Lenschow et al. 1974; Heymsfield et al. 1979; Harmer et al. 1990).

On an enlargement of one of these cloud penetrations (Fig. 11), temperature measurements obtained by the AUSAT is compared to those from a prototype of a very fast thermometer built by Météo France (Villain et al. 1996). This last thermometer, also experimented during these flights, uses a very thin tungsten wire (5- $\mu$ m diameter) placed in a small cylindrical housing and protected from water droplets by an helicoidal device.

The thin-wire thermometer was mounted on the front part of the fuselage, but unfortunately, not on the same side as the AUSAT. Both signals display fluctuations of the same amplitude, which appear to have physical significance. But, some discrepancies can be seen between the two signals. They are due to the high resolution of the two thermometers, which do not catch the same phenomena at their two different locations.

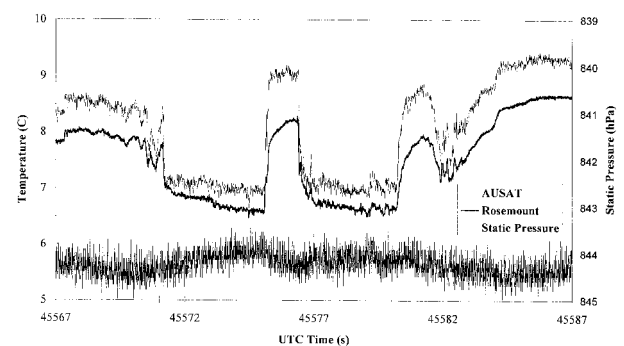


FIG. 10. Same time series of AUSAT and Rosemount temperatures with the radome static pressure probe. (Same flight and same rate as in Fig. 9.)

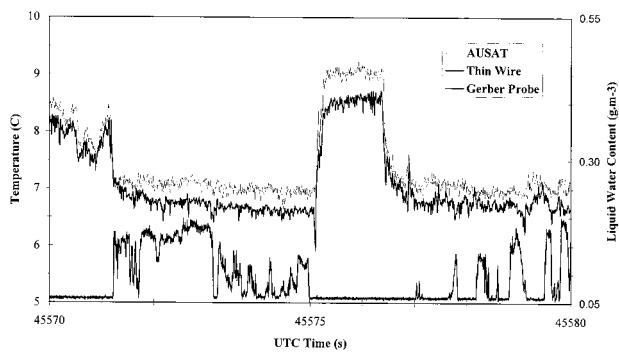


FIG. 11. Expanded portion on 10 s of the same time series of AUSAT and Rosemount temperatures with the PMV 100 Gerber probe liquid water content. (Same flight and same rate as in Fig. 9.)

As may be seen in Fig. 11, the thin-wire thermometer has a double time constant, probably due to its housing as for the Rosemount (Rosemount Engineering Company 1965; Lawson 1988; Harmer et al. 1990).

Furthermore, at the end of the penetration, the thin-wire thermometer record shows a spike, which could be interpreted as an evaporative cooling one.

*b. Estimate of the AUSAT response time from time series*

Figure 12 is an enlargement of another cloud penetration performed during spring 1997. These data concern a time period of 1.5 s (each graduation corresponds to 0.05 s). From these data, the measured AUSAT response time appears smaller than 50 ms. The Rosemount and the Météo France's thin wire present a comparable double response time, in the order of 1 s, due to their housing.

*c. Soundings*

AUSAT and Rosemount temperature during a sounding are shown from 1020 to 700 hPa (Fig. 13). Once

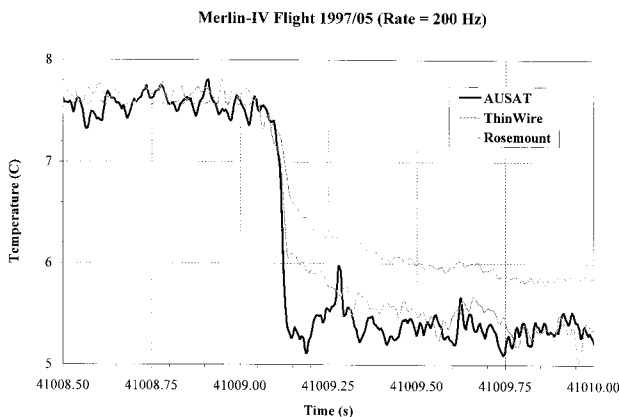


FIG. 12. Expansion, after adjustment, of 1.5 s of high rate time series of AUSAT, thin wire, and Rosemount temperatures through a sharp cloud exit. (Same flight and same rate as in Fig. 9.)

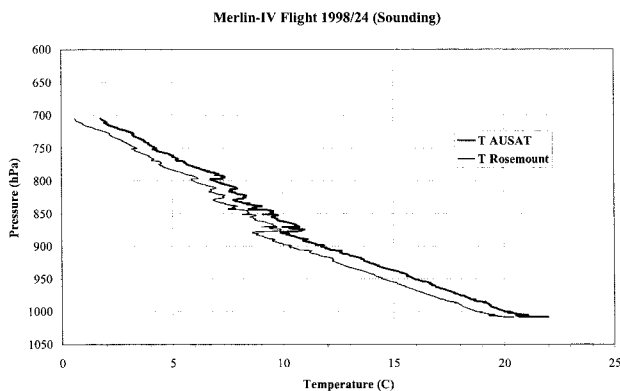


FIG. 13. AUSAT and Rosemount temperature profiles in a sounding flight.

again, AUSAT data are not linearly corrected to fit Rosemount data in clear air.

Most recent data from the TRAC 98 experience, show that AUSAT data are linearly correlated with Rosemount data following this relation (B. Piguet of Météo France 1998, personal communication):

$$T_{AUSAT} = 0.95T_{Rosemount} + 0.85.$$

In this relation,  $T_{AUSAT}$  is already humidity corrected. So, adjusting the AUSAT temperature to fit the Rosemount one may be done by the inversion of the last formula,

$$T_{AUSATadjusted} \approx 1.05T_{AUSAT} - 0.89.$$

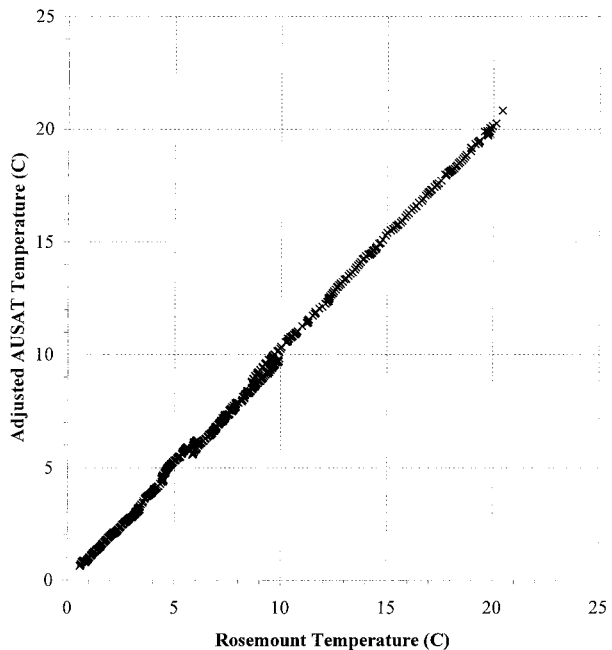


FIG. 14. Comparison of the measurement of temperature from the adjusted AUSAT and Rosemount probes, each point represents the average of 200 samples spanning 1s. (Same flight and same rate as in Fig. 13.)

Figure 14 compares both temperatures after adjustment. Before it, AUSAT data overestimated temperatures under 18°C and underestimated them over 18°C.

*d. Estimate of the AUSAT response time and band pass from power spectra*

From homogeneous turbulence theory, power spectra of an atmospheric variable should follow the expected  $-5/3$  power ratio. Power spectra of different sensors are shown in Fig. 15 together with  $(-5/3)$  slope straight lines. Spectra have been smoothed (on six iterations) using a 1024-point Hamming window on the same time series.

Figures 15a and 15b show the Rosemount 102 and the Lyman- $\alpha$  spectra respectively with a bandwidth of 20 and 40 Hz. Data from this hygrometer are used for AUSAT humidity correction. One should note the exceedingly steep slope of the Rosemount spectrum, which implies that temperature given by this probe should not be used at frequencies higher than a few hertz.

The third spectrum (Fig. 15c) concerns the AUSAT data before the humidity correction, filtered at 50 Hz by the output filter. The fourth spectrum (Fig. 15d) is for the same AUSAT data but after humidity correction by the Lyman- $\alpha$  data. The similarity of the two last spectra shows that a very little noise is added by the humidity correction. For this sample, the bandwidth is better than 30 Hz. Practical response time may be deduced from these spectra by taking the inverse of the bandwidth equal to 33 ms.

*e. AUSAT in-cloud temperature measurement*

It has been said that sonic anemometers–thermometers should not work at all in cloudy air: large signal lessening due to considerable absorption and diffusion by cloud droplets, reduced sound velocity inducing temperature underestimation by several degrees. The data presented in Figs. 9, 11, and 12 show that the AUSAT works and its temperature is very comparable to those of Rosemount and thin-wire sensors.

However, comparing in-cloud and out-cloud AUSAT temperature to the Rosemount and to the Météo France's thin wire, it can be observed that amplitude variation of AUSAT temperature seems greater than the Rosemount one but absolutely comparable to the thin-wire one. Thus, taking into account that, before entering the clouds, the AUSAT temperature is greater than the Rosemount by 0.55°C, the in-cloud AUSAT temperature appears lower than Rosemount by about 0.50°C. Of course, it is well known that Rosemount cannot really be considered as a reference for in-cloud temperature measurements: it is supposed to be sometimes lesser by several tenths of degrees (up to 1.9°C) than the real temperature, due to evaporative cooling of droplets trapped by the sensing element (Harmer et al. 1990; Lenschow and Pennel 1974).

However, one may question whether a possible evaporative cooling of the cloudy air in the AUSAT measurement channel may be due to the slowdown. An estimation of the possible effect of cloud droplet evaporation on temperature in the measurement channel can be made by taking into account the dynamic heating correction for AUSAT probe and a diagram giving the theoretical lifetime of an evaporating drop as a function of its radius and of the relative humidity of the environment (Lawson 1988). This diagram is based on a very classic hypothesis and theory of microphysics (Pruppacher and Klett 1980), in particular on the fact that the growth of the evaporation of a cloud droplet is a rather slow process due to the low diffusion velocity of water molecules through oxygen and nitrogen molecules.

Let the in-cloud temperature be equal to 6.5°C, the mean static pressure  $P = 844.3$  hPa, and  $q = 6.3$  g kg $^{-1}$  (as measured by the Lyman- $\alpha$  hygrometer). We obtain an humidity of 88.4%, indicating an initial in-cloud subsaturation of 11.6% (at saturation  $e_w = 9.67$  hPa and  $r_w = 7.12$  g kg $^{-1}$ ). This subsaturation may perhaps be explained by the fact that we are near the cloud top where entrainment and mixing are important. The 4.33°C dynamic increase of temperature inside the cylinder yields to an hygrometry of 65.8%, thus to a subsaturation of 34.2%.

Figure 16 shows that for droplets whose radius is 5  $\mu\text{m}$  the evaporation time lays between 1 and 8 s for relative humidity ranging between 20% and 90%. For droplets of 20  $\mu\text{m}$  this time varies from 12 to more than 80 s for the same range of humidity. As the flow within the AUSAT is about 40 m s $^{-1}$ , assuming evaporation on a 40-cm path (crossing time of 10 ms), it may be inferred that there is not enough time for droplets to totally evaporate. By writing the time constant evaporation  $\tau_r$ ,

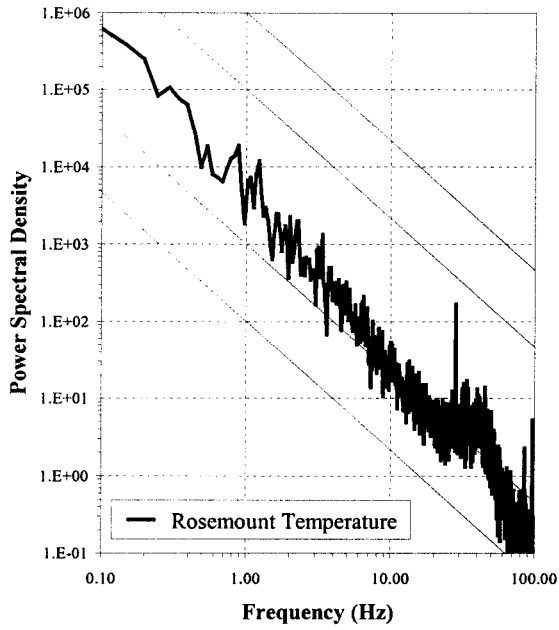
$$\tau_r = \frac{1}{\frac{1}{r} \frac{dr}{dt}}$$

We can calculate that for time  $t$ , a droplet of initial radius  $r_o$  and mass  $m_o$  falls to a radius  $r$  and a mass  $m$  such as

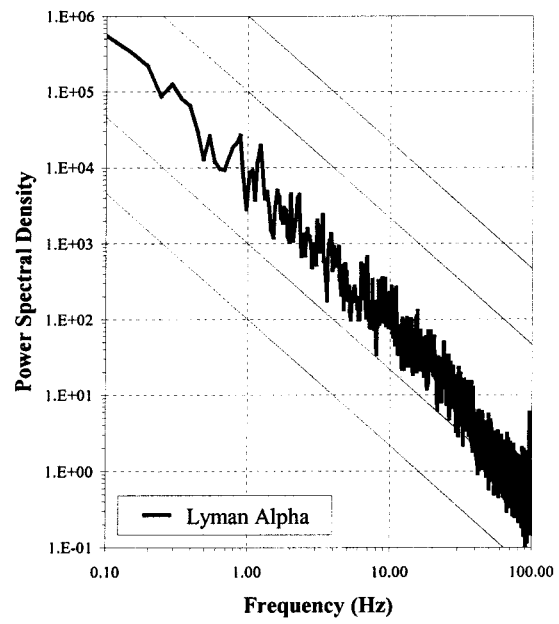
$$r = r_o \exp\left(-\frac{t}{\tau_r}\right) \Leftrightarrow m = m_o \exp\left(-\frac{3t}{\tau_r}\right).$$

From the diagram, for an initial radius  $r_o = 5$   $\mu\text{m}$  and a relative humidity  $\approx 70\%$ , the time constant is  $\tau = 3$  s. As the crossing time  $t = 10$  ms, we obtain  $m/m_o = 0.990$  that is a relative variation of mass of 1% and  $r/r_o = 0.997$ . With a measured liquid vapor content of 0.25 g kg $^{-1}$ , the evaporated water is in the order of  $2.5 \times 10^{-3}$  g kg $^{-1}$ , resulting in an evaporative cooling of about  $6 \times 10^{-3}$ °C. Thus, if the classical theory from which this diagram is deduced may be applied to AUSAT, although some hypothesis have not been complied

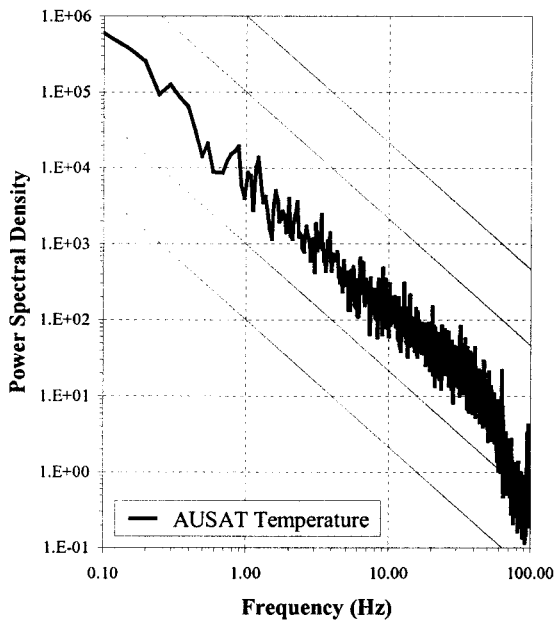
### Merlin-IV Flight 1996/31 (Rate = 200 Hz)



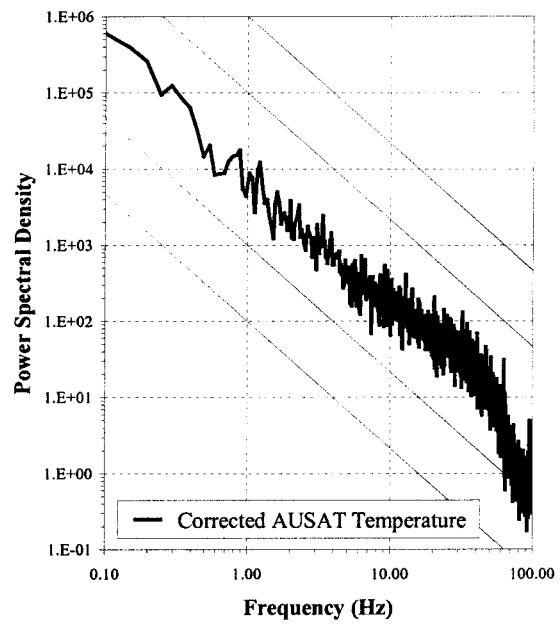
*a*



*b*



*c*



*d*

FIG. 15. Power spectra for Rosemount temperature, Lyman- $\alpha$  humidity, noncorrected, and corrected AUSAT temperature for the same time series sampled at 200 Hz and smoothed with a 1024-point Hamming window; solid lines are of slope  $-5/3$ .

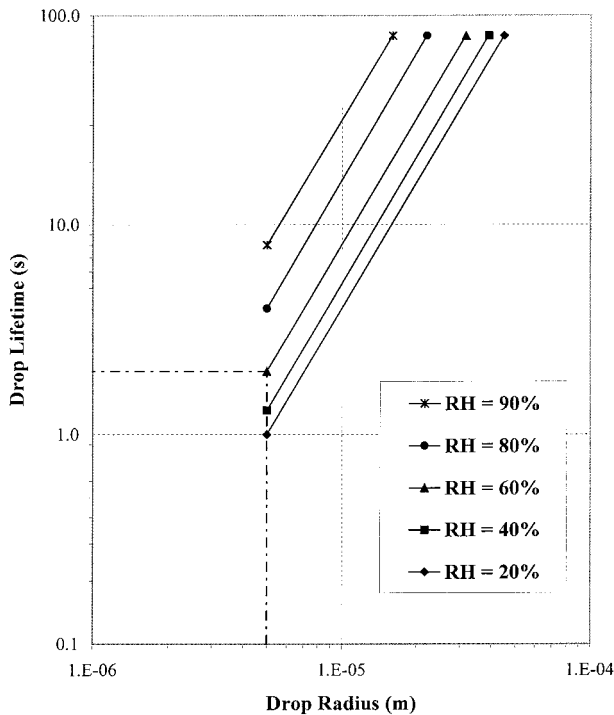


FIG. 16. Relationship showing the theoretical lifetime of an evaporating drop as a function of drop radius and relative humidity of the environment (from Lawson 1988).

with (droplets at rest, stationarity), this effect cannot be invoked in order to explain the observed difference between in-cloud AUSAT and Rosemount temperatures.

Even with greater liquid water content, (up to  $1 \text{ g kg}^{-1}$ ) this variation of drop mass does not seem to have an effect on the measurement (cooling up to  $2.5 \times 10^{-2} \text{ }^\circ\text{C}$ ). In an evaporative process, only the droplet is essentially cooling down, due to the low thermal diffusivity of the air. Thus, it is highly probable that, even for larger partial evaporation, the very short time taken by the droplet to cross the cylinder does not allow a sensible cooling of the cylinder air bulk.

But now, it is interesting to consider the humidity correction applied to the AUSAT data. Out of cloud, humidity  $q$  is on the order of  $3 \text{ g kg}^{-1}$ , yielding to  $\Delta T_o = 0.43^\circ\text{C}$ . The in-cloud value of  $q$ , as measured by the Lyman- $\alpha$  hygrometer, is equal to  $6.3 \text{ g kg}^{-1}$ , yielding to  $\Delta T_o = 0.91^\circ\text{C}$  (by taking  $q_w = 7.12 \text{ g kg}^{-1}$  we would find  $\Delta T_o = 1.03^\circ\text{C}$ ). Before humidity correction, AUSAT data always remain above Rosemount. So, we can see that the observed difference of  $0.5^\circ\text{C}$  between AUSAT and Rosemount in-cloud temperatures may be explained by the strong change in humidity observed when the aircraft penetrates the cloud.

Moreover, according to some authors (Lenschow 1986; Hartman et al. 1990), in some cases of high hygrometry, Rosemount temperature data may also be higher than the correct temperature when salt crystals are trapped on the sensing element. This salt becomes

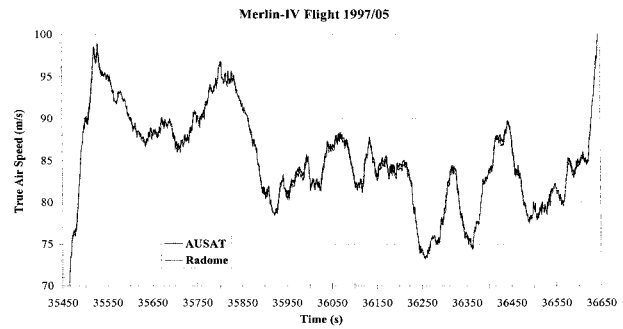


FIG. 17. Time series of the true airspeed of the aircraft measured by the AUSAT and calculated with classical equation from radome gust probe data.

deliquescent before saturation is reached and increases the probability of the occurrence of sensor wetting: condensation on the sensor and corresponding latent heat deposition may result in temperature higher than the correct of several tenths of degrees. These possibilities of contamination errors are pointed out by Rosemount Inc. (Stickney et al. 1981).

So, if the uncertainty on in-cloud Rosemount temperature is assumed to be in the order of  $\pm 1^\circ\text{C}$ , then the observed  $0.5^\circ\text{C}$  in-cloud deviation between AUSAT and Rosemount data remains in the uncertainty domain of Rosemount in-cloud measurement. However, we are aware that some more complete theoretical and practical investigations are to be conducted before we know all the possible errors in our in-cloud temperature measurement.

#### f. AUSAT true airspeed measurement

On board the Merlin IV, the true airspeed is calculated from data measured by dynamical and thermodynamical sensors such as a five-hole radome and an impact thermometer (Brown et al. 1983). Complete calculation of true airspeed needs data provided by several other instruments generally with a very different response time and bandpass, so that even if they are, at last, delivered at 200 Hz, the classic true airspeed data do not constitute a fast measurement of this parameter, nor an absolute reference (Nacass 1992). Approximation of measurements of static temperature, static and dynamic pressures, position error, angles of attack and sideslip, and by neglecting the air humidity (Khelif et al. 1999), induce an estimation of accuracy on the calculation of the true airspeed that may reach up to  $1 \text{ m s}^{-1}$  (Morera 1995).

The AUSAT airspeed, compared to the classical measurement (Fig. 17), shows that the two determinations are very close. For example, for an airspeed varying between 75 and  $95 \text{ m s}^{-1}$ , the difference remains under  $0.40 \text{ m s}^{-1}$  (Fig. 18). There is no direct correlation between the AUSAT true airspeed and the angles of attack and sideslip (Figs. 19, 20) except the correlation from

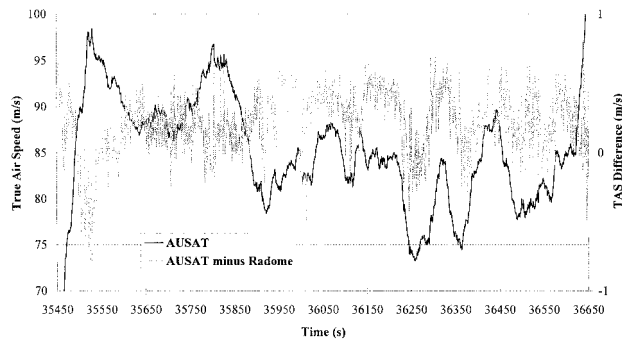


FIG. 18. Time series of the true airspeed of the aircraft measured by the AUSAT and of the difference between the true airspeed of AUSAT minus that of radome. (Same flight and same rate as in Fig. 17.)

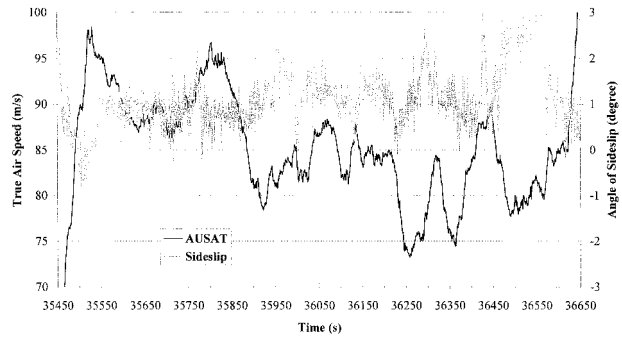


FIG. 20. Time series of the true airspeed of the aircraft measured by the AUSAT and of the angle of sideslip measured by the radome differential pressure probe. (Same flight and same rate as in Fig. 17.)

the dynamics of flight (Etkin 1972). The same conclusion can be drawn about the correlation between these two angles and the difference between the AUSAT true airspeed and the radome one (Fig. 21) where the variations are under the limit of a real influence.

So, the AUSAT corroborates the rather complicated algorithm used in atmospheric research for the true airspeed determination and provides a different and very simple way to obtain, at high frequency, a precise value of the true airspeed.

*g. Characterization of adiabatic ascents in a convective planetary boundary layer*

In order to test thermometer performances, a calibration flight is used. It was performed during a pre-ACE-2 field experiment calibration flight, in June 1997, above the Beauce Plain in France. The Merlin IV flew through updrafts of a slightly convective boundary layer with cumulus clouds. The adiabatic updrafts are identified thanks to the total water mixing ratio  $r_t$  ( $\text{kg kg}^{-1}$ ).

With the water evaporation/condensation latent heat  $L$  ( $\text{J kg}^{-1}$ ) and the liquid water mixing ratio  $r_1$  ( $\text{kg kg}^{-1}$ ), the liquid water potential temperature  $\theta_1$  (K) is calculated with the following formula:

$$\theta_1 = \theta \exp\left(-\frac{Lr_1}{C_p T}\right).$$

The test consists in comparing three liquid water potential temperatures. The first,  $\theta_{1A}$ , is computed from AUSAT temperature; the second,  $\theta_{1R}$ , from the Rosemount probe temperature; and the third value is deduced from adiabatic invariance. For this flight, the AUSAT temperature is linearly corrected in order to fit the Rosemount probe temperature in clear air by the formula (see section 8c):

$$T_{\text{AUSATCorrected}} = 1.03T_{\text{AUSAT}} - 0.9.$$

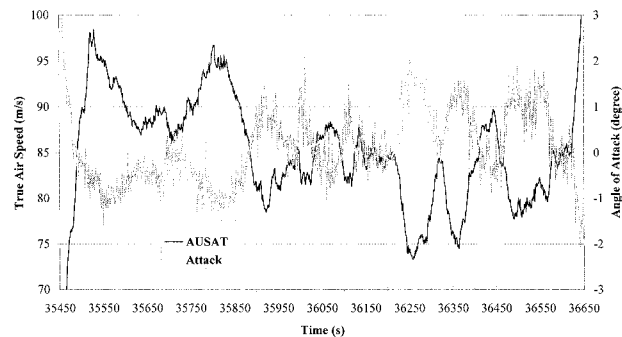


FIG. 19. Time series of the true airspeed of the aircraft measured by the AUSAT and of the angle of attack measured by the radome differential pressure probe. (Same flight and same rate as in Fig. 17.)

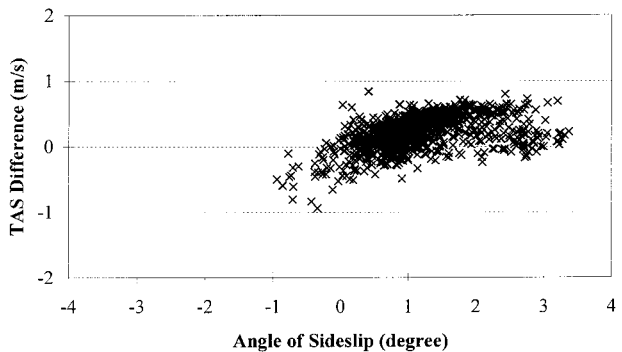
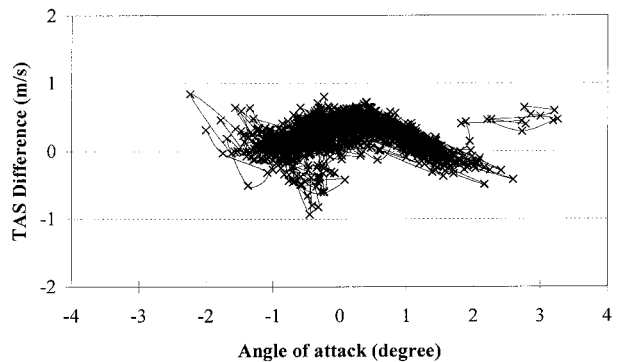


FIG. 21. AUSAT true airspeed minus radome true airspeed plotted as a function of the angles of attack and sideslip. (Same flight and same rate as in Fig. 17.)

## Merlin-IV Flight 1997/11 (Rate = 200 Hz)

Leg 1 : 1550m

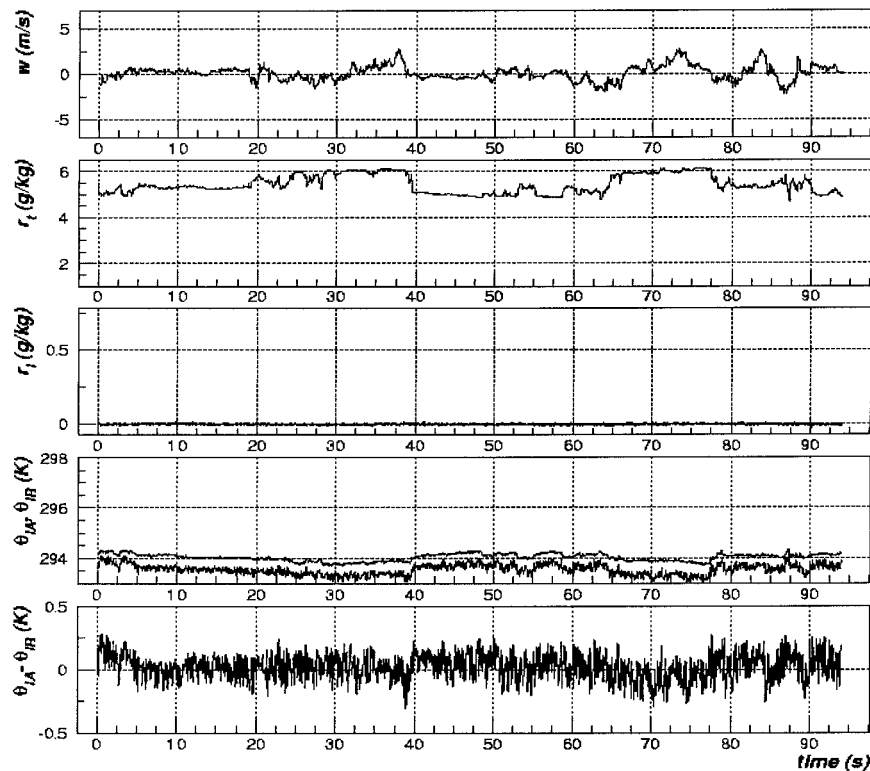


FIG. 22. Time series of thermodynamic data recorded at the altitude of 1550 m, under the cumulus cloud base at the upper part of the boundary layer.

Average conditions near ground level at 1006 hPa were a potential temperature  $\theta_g = 295$  K and a mixing ratio  $r_g = 6.3$  g kg<sup>-1</sup>. The vertical air velocity computed by the Merlin IV is noted as “w” (m s<sup>-1</sup>).

Five legs were performed consecutively at altitudes of 1550, 1700, 2000, 2300, and 2450 m and at the aircraft speed nearby 100 m s<sup>-1</sup>. The first leg was run in clear air under the cloud bases, the second near condensation level, the third and fourth across clouds, and the last one at cloud top. Figures 22–25 display, versus the time in seconds, for each of these legs:  $w$ ,  $r_l$  and  $r_i$ ,  $\theta_{lA}$ ,  $\theta_{lR}$  and  $\theta_{lA} - \theta_{lR}$ . Notice that  $\theta_{lA}$  and  $\theta_{lR}$  are displayed on the same graph, the latter being offset by 0.5 K.

On the two lower level plots (Figs. 22, 23) the upper part of the boundary layer appears highly heterogeneous: broad areas of nearly uniform  $r_i$  ( $\approx 6$  g kg<sup>-1</sup>) are separated by chaotic areas with  $r_i$  values ranging from 4.5 to 5.5 g kg<sup>-1</sup>. In high  $r_i$  areas, liquid water potential temperature  $\theta_l$  is also nearly uniform ( $\approx 293.5$  K) while vertical air velocity is positive and in the order of 1–2 m s<sup>-1</sup>. These areas may be interpreted as well-formed homogeneous updrafts expected to raise adiabatically up to some level above which entrainment will yield

mixtures with lower  $r_i$  and higher  $\theta_l$ . Two such drafts are visible in the first leg plot and four in the second one, among which three display a small amount of liquid water ( $r_l \approx 0.05$  g kg<sup>-1</sup>). In adiabatic ascents, total water mixing ratio and liquid water potential temperature have to be constant; the first two leg results are consistent with an adiabatic ascent mixing ratio ( $r_a \approx 6 \pm 0.1$  g kg<sup>-1</sup>) and both thermometers agree with an adiabatic ascent liquid water potential temperature ( $\theta_a \approx 293.5 \pm 0.1$  K).

On the third leg (Fig. 24), the aircraft penetrated a cumulus cloud ( $r_i \approx 0.4$  g kg<sup>-1</sup>) 300 m above its basis. Again,  $r_i$  reaches  $r_a$ , which is compatible with an adiabatic updraft. Here,  $\theta_{lR}$  and  $\theta_{lA}$  are both within 0.1 K of  $\theta_a$ .

In the next higher-level leg (Fig. 24),  $r_i$  reaches only 5.5 g kg<sup>-1</sup> during cumulus cloud penetration suggesting some entrainment and mixing at this level. For both thermometers,  $\theta_l$  hardly passes below 294 K. A clear updraft is also crossed in which  $r_i$  reaches 4 g kg<sup>-1</sup> and  $\theta_l$  294.8 K.

In the last leg (Fig. 25), the aircraft flew through the cumulus cloud top. The updraft with the strongest mixing ratio ( $4 \leq r_i \leq 5$  g kg<sup>-1</sup>) and the lowest liquid water

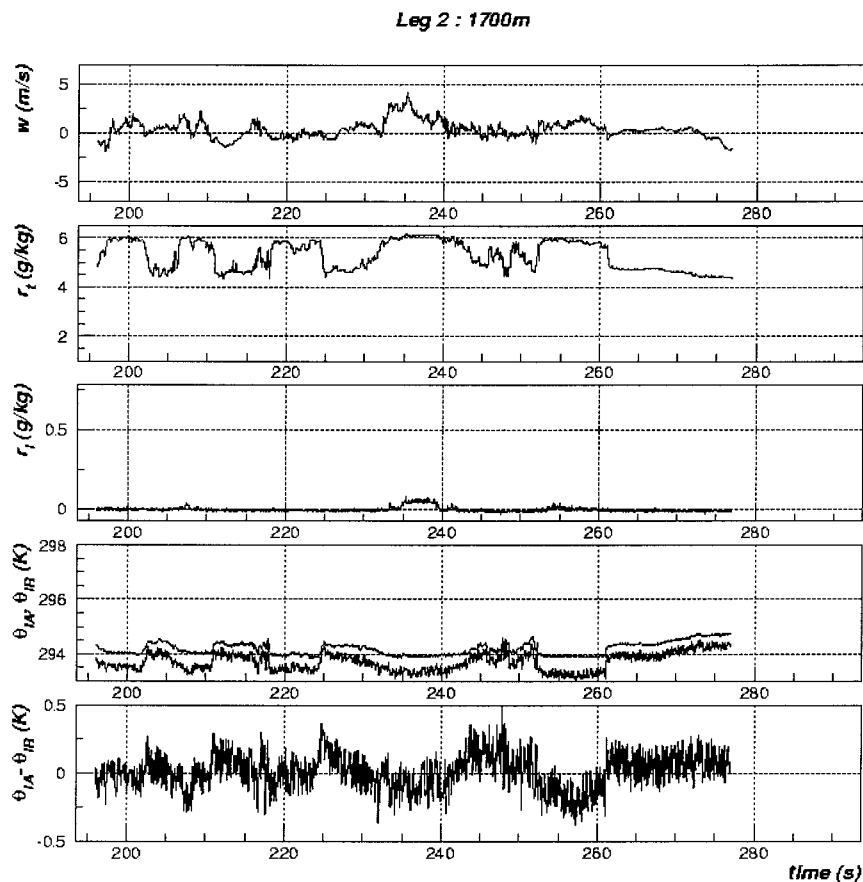


FIG. 23. Time series of thermodynamic data recorded at the altitude of 1700 m at the cumulus cloud base. (Same flight and same rate as in Fig. 22.)

potential temperature ( $295 \leq \theta_1 \leq 295.8$  K) is surrounded by two well-defined downdrafts with minimal  $r_l$  (1 and  $1.5 \text{ g kg}^{-1}$ ) and maximal  $\theta_1$  ( $\approx 297$  K).

In all this flight, the same general features are observed as in the next in 1998:

- Globally, the AUSAT performs correctly: the temperature difference with the Rosemount stays below 0.2 K, except in a few points.
- The AUSAT variability is higher than the Rosemount one; high-frequency fluctuations account for  $\pm 0.1$  K; sharp temperature variations (1 or 2 K in less than 0.5 s) induce temperature differences reaching 0.5 K (e.g., legs 3 and 4 at times  $t = 407$  s and  $t = 583$  s); temperature fluctuations with a characteristic time of 1 or 2 s induce temperature differences  $\pm 0.2$  K (leg 3,  $405 \text{ s} < t < 425 \text{ s}$ ).
- In-draft temperatures given by the AUSAT are lower than those given by the Rosemount.

In addition, in-draft temperatures from both thermometers are compatible with the adiabaticity given by  $r_l$  measurements.

Thus, this test would look quite satisfactory, were it not for the cold bias of the AUSAT relative to the Ro-

semount. This bias is manifest in two instances: in clouds, and in clear but humid updrafts.

The first point, which was already analyzed in section 8e, can be examined more closely. It turns out that the temperature differences are larger when  $r_l$  is low ( $r_l < 0.2 \text{ g kg}^{-1}$ ). See, for instance, cloud crossing of leg 4, where  $r_l$  decreases with time, while the absolute value of the difference  $\theta_{1A} - \theta_{1R}$  increases). Especially during leg 2, where liquid water amounts involved in updrafts are very low ( $< 0.05 \text{ g kg}^{-1}$ ), the temperature differences lie between 0.3 and 0.4 K. The second point appears clearly, for instance, at times 595–598 s (leg 4) when the aircraft flies through a clear updraft: the AUSAT temperature drops by 1.5 K while the Rosemount temperature drops only by 1.1 K.

It seems very difficult to disentangle the contributions of the two thermometers to these biases. The present observations would be compatible with the Rosemount being too slow to follow fast temperature changes and being polluted by salt and thus warmed up by condensation when humidity is close to saturation. Also, neither evaporative cooling of the AUSAT measurement channel, nor sound velocity change by cloud drops, would make the AUSAT temperature colder when little liquid

## Legs 3 and 4 : 2000m and 2300m

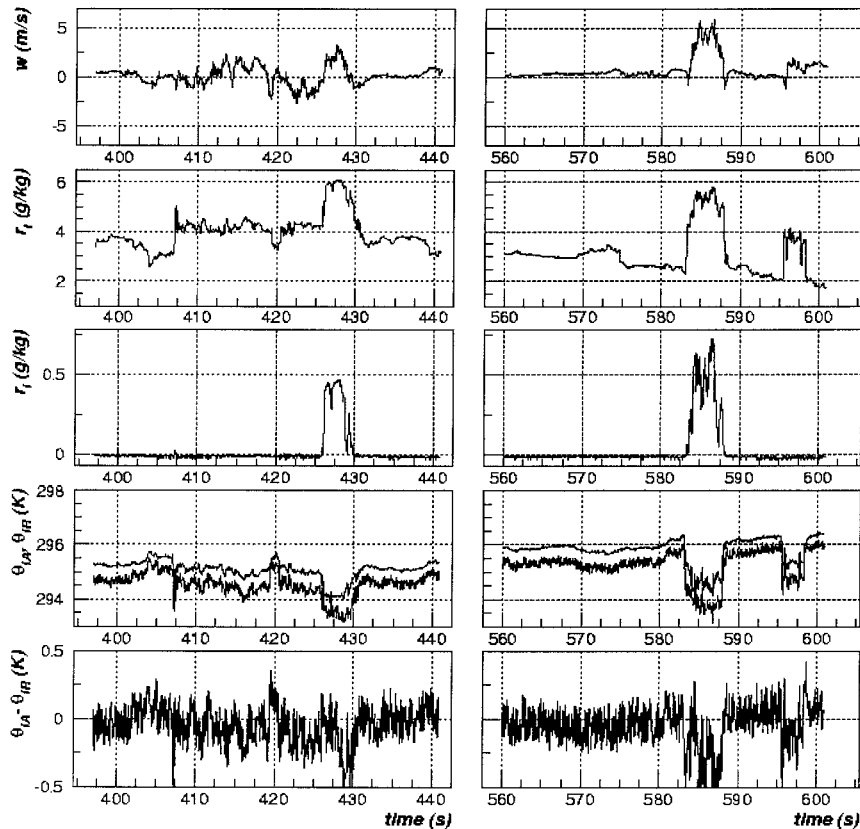


FIG. 24. Time series of thermodynamic data recorded at the altitudes of 2000 and 2300 m, in a cumulus cloud penetration, 300 and 600 m above the cloud basis. (Same flight and same rate as in Fig. 22.)

water is present compared to situations when  $r_1$  is large. On the other hand, since the cold bias manifests itself even in clear humid drafts, one will have to investigate the effect of different gas laws on the behavior of sound velocity when humidity varies, even though such deviations from usual perfect gas law are not mentioned in studies of ground-based sonic thermometers.

To sum up, during this 1997 test flight the AUSAT provided fast and accurate temperature. Improving still its accuracy will demand understanding the discrepancies between AUSAT and Rosemount probe, which will require new field experiments with increased care, especially preventing pollution of the Rosemount probe by salt. Behavior of sound velocity in mixtures of air and water vapor also need to be investigated.

## 9. Discussion and conclusions

The sound wave propagation theory given here above is a very elementary one since it is supposed that air is an ideal gas. Viscosity and the presence of cloud droplets have not been taken into account. These hypotheses, which seem reasonable in almost all the classic mete-

orological applications of physics, have to be justified in the case of metrology.

Practically, there are a lot of secondary effects which necessarily induce a slight deviation of measured sound velocity relative to the theoretical one as obtained by the elementary theory. In fact, number of these effects may be neglected since this thermometer is designed to be a robust sensor for temperature fluctuation measurements and not a temperature reference.

In dry air, viscosity and thermal conductivity produce an attenuation which is proportional to the square of the wave sound frequency. According to Kinsler (1982), these effects are insignificant at 120 kHz, the resonance frequency of the emitters.

In presence of water vapor, the molecular relaxation phenomenon produces a noticeable sound attenuation and a slight modification of sound velocity, but essentially in the audible frequency range (Harris 1971; Morse and Ingard 1986). For frequencies larger than 100 kHz the effects of molecular relaxation can be completely neglected (Harris 1971). However, in the case of a simultaneous high concentration in carbon dioxide and in water vapor in altitude, this relaxation phenom-

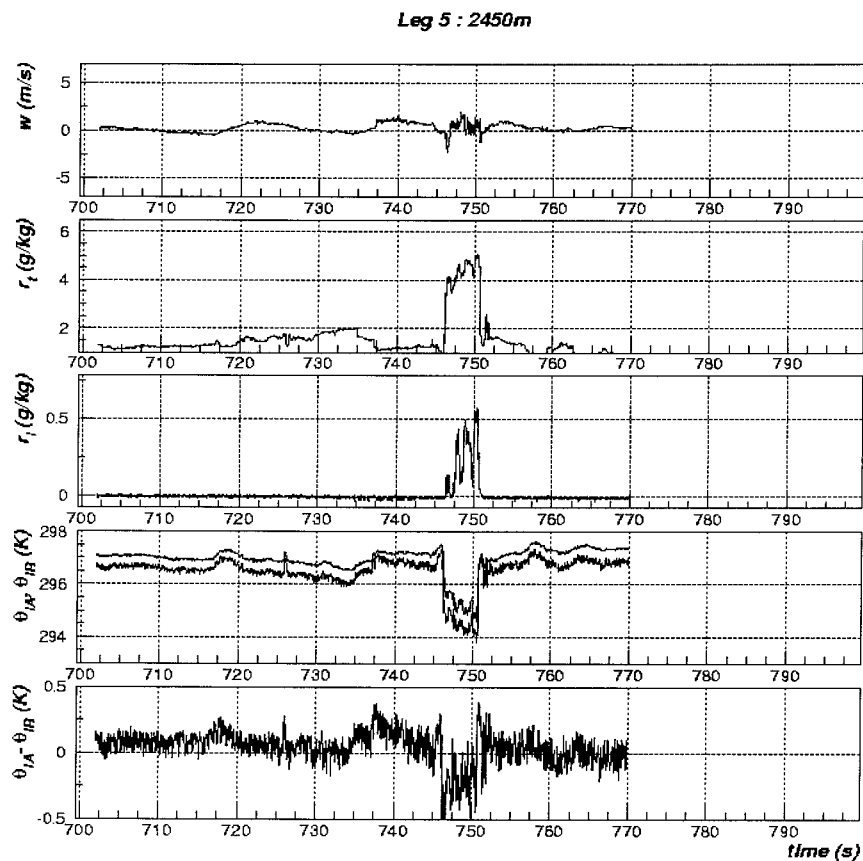


FIG. 25. Time series of thermodynamic data recorded at the altitude of 2450 m at the cumulus cloud top. (Same flight and same rate as in Fig. 22.)

enon can introduce significant errors in temperature determination by means of a sonic thermometer (Kinsler 1982).

As shown in the section 8 for high humidity, the formula (6) used for humidity correction (commonly accepted in classical ground-based sonic thermometers) has probably to be improved by coupling further theoretical and experimental studies.

In cloudy air, theoretical study of sound propagation is complicated by the presence of cloud water droplets in variable concentration and granulometry. Thus, one may expect attenuation and dispersion of sound waves by phenomena such as diffraction by cloud droplets or as displacement of cloud droplets themselves by the traveling sound wave. Taking into account the relative small size of cloud droplets (generally less than  $20 \mu\text{m}$  in nonprecipitating clouds) compared to the used wavelength ( $2.7 \text{ mm}$ ) diffraction is negligible. Due to the rather low concentration of droplets in cumulus and stratocumulus cloud (roughly  $100 \text{ cm}^{-3}$  in oceanic air masses and  $600 \text{ cm}^{-3}$  in continental air masses) and the short length of the measurement pass, attenuation is very weak. And fortunately, according to Knudsen (1948), the effects of the displacement of cloud droplets are of the second order.

The problem of the very rapid heating of the air in the measurement channel seems a little less troublesome. This heating may be supposed to induce a partial evaporation of the cloud droplets in the channel and a possible evaporative cooling of the inner air, that may alter the temperature correction due to the slow down. Nevertheless, considering that at an airspeed of  $100 \text{ m s}^{-1}$ , a cloud droplet crosses the measurement channel in about 10 ms, it may be expected that the evaporation process has no time to be really efficient. Indeed, in cloud physics, it is generally assumed that the growth or the evaporation of a cloud droplet is a rather slow process, due to the low diffusion velocity of water molecules through oxygen or nitrogen molecules. Moreover, in an evaporating process, it is essentially the droplet that cools down. Taking into account the low thermal conductivity of the air, it is highly probable that, even if a partial evaporation is present, the very short time taken by the droplet to cross the cylinder does not allow a sensible cooling of the cylinder air bulk.

This hypothesis is also supported by the experimental work of Knudsen (1948), on sound propagation in smog and the so-called thermal relaxation process. Due to successive adiabatic compression and expansion of the air when the sound wave is traveling, slight changes in

temperature induce evaporation and condensation of water droplets. At very low frequencies, sound is strongly attenuated and dispersed. This effect is maximum at 500 Hz and then decreases rapidly with increasing frequencies due to the time constant of the evaporation and condensation processes.

Another effect that has not been taken into account is the effective presence of a fluctuating boundary layer at the immediate vicinity of the cylinder wall. A theoretical approach of this problem has shown that deviation may be disregarded.

In conclusion, although the in-cloud AUSAT behavior in high-humidity areas needs further investigations, its weak sensitivity to water droplets and its very fast response time can provide a noticeable improvement in airborne temperature measurements to estimate the entrainment of surrounding air into a growing cumulus (Heymsfield et al. 1979) and also to calculate the turbulent fluxes (Smith and Jonas 1995).

*Acknowledgments.* This study was first funded by the Ministère des Armées/DRET (Direction des Recherches et Techniques) then, on several occasions, by the CNRS/INSU (Institut National des Sciences de l'Univers).

The present prototype was built, partly in the Division Prototype of the Université de Paris 6—Pierre et Marie Curie, and in the Division Projet of the LMD (Laboratoire de Météorologie Dynamique du CNRS).

The Département Aérodynamique of the ONERA (Office National d'Etudes et de Recherches Aérospatiales) gave us very precious help in the aerodynamic definition of the sensor. In addition, the tests in the ONERA wind tunnel of Chalais–Meudon were decisive for our understanding of the acoustic phenomenon limiting sensor performances.

Many encouragements and valuable advice were given by the Division Technique of the INSU, during a lot of test flights performed on board the Fokker 27—ARAT (Avion de Recherche et de Télédétection Atmosphérique). Some of these tests were sometimes very disappointing for us!

For the flights on board the Merlin IV, we would like to acknowledge all the crew and all the team of the Météo France/CNRM/CAM (Centre d'Aviation Météorologique, one facility of the Centre National de Recherches Météorologiques) for their friendly reception and continuous help, as well as for mounting the AUSAT on board of the aircraft, as for processing the data treatment.

Thanks too, to M. Zephoris and J. Villain of the Météo France/SETIM (Service des Equipements et des Techniques Instrumentales de la Météorologie) who permitted us to use not yet published data from their thin-wire thermometer.

Many thanks to B. Piguet of the Météo France/CNRM/GMEI (Groupe de Météorologie Expérimentale et Instrumentale) and D. Picard of the LMD for their help in data processing.

We wish especially to thank A. Druilhet (Laboratoire d'Aérodynamique of the Université Paul Sabatier de Toulouse) for numerous helpful discussions on signal processing and his constant encouragement.

We gratefully acknowledge the contribution of E. Hicks (Université Antilles-Guyane) in microphysics. The authors also wish to say un grande merci for the constructive input of the anonymous reviewers.

## APPENDIX A

### Theoretical Background

#### a. Elementary theory of sound propagation

Assuming that sound propagation is an adiabatic phenomenon and that the air is a dry ideal gas, then the local value of the speed of propagation of sound waves  $c$  is given by

$$c^2 = \gamma_a \frac{\bar{P}}{\bar{\rho}_a} = \gamma_a R_a \bar{T} = \left( \frac{\partial P}{\partial \rho} \right)_s,$$

where  $\bar{P}$  and  $\bar{T}$  are, respectively, the pressure (Pa) and the temperature (K) of the undisturbed air,  $\bar{\rho}_a$  is the dry air density ( $\text{kg m}^{-3}$ ),  $\gamma_a = c_{pa}/c_{va}$  the ratio of specific heats of dry air, and  $R_a$  is the specific constant of dry air.

The fluid is moving at a constant entrainment velocity  $\mathbf{V}$  relative to an emitter–receiver couple. Then, the absolute velocity  $\mathbf{V}_a$  is given by

$$\mathbf{V}_a = \mathbf{c} + \mathbf{V}.$$

The wave perturbation emitted by E1 at the time  $t = 0$ , in the direction defined by  $\mathbf{c}$ , reaches the receiver R1, at the time  $t_1$  from the corresponding virtual source E''1:

$$t_1 = \sum_i \delta t_i \Rightarrow \mathbf{c}t_1 + \mathbf{V}t_1 = \mathbf{V}_a t_1 = \mathbf{L}_1 \quad \text{with } L_1 = L.$$

With the sine rule in this general triangle, it is easy to write

$$\frac{L_1}{\sin \alpha_1} = \frac{ct_1}{\sin 45} = \frac{Vt_1}{\sin \beta_1}.$$

Thus,

$$\sin \beta_1 = \frac{\sqrt{2}}{2} \frac{V}{c} \quad \text{and} \quad \alpha_1 = 135 - \beta_1.$$

In the same way, the ray propagation may be defined for the upwind path (Fig. A1) as

$$t_2 = \sum_j \delta t_j \Rightarrow \mathbf{c}t_2 + \mathbf{V}t_2 = \mathbf{V}_a t_2 = \mathbf{L}_2 \quad \text{with } L_2 = L.$$

Again using the sine rule in a general triangle,

$$\frac{L_2}{\sin \alpha_2} = \frac{ct_2}{\sin 135} = \frac{Vt_2}{\sin \beta_2}$$

$$\sin \beta_2 = \frac{\sqrt{2}}{2} \frac{V}{c} = \sin \beta_1 \Rightarrow \beta_1 = \beta_2 = \beta$$

$$\alpha_2 = 45 - \beta = \alpha_1 - 90.$$

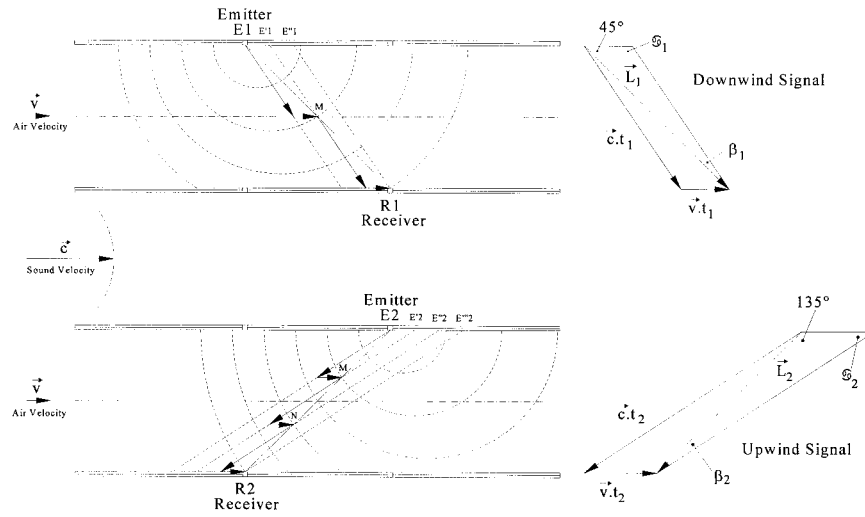


FIG. A1. Geometry of wave propagation along the downwind and upwind AUSAT paths.

Note that, in order to obtain the best signal, the transducers of the downwind path have to be oriented along the E'1–R1 direction and those of the upwind path along of the E''2–R2 direction. Indeed, transducers have a highly directive energy diagram to avoid spurious reflections on the inner wall of the sensor.

*b. Geometry of the volume of measurement*

As shown in Fig. 4, the emitter–receiver transducers (E1, R1, E2, and R2) are located on four of the eight vortices of the cuboid (E1–R2–R3–E4–R1–E2–E3–R4) fitted in the sensor's inner cylinder. This cuboid is the measurement volume and has two opposite square faces (E1–R2–R4–E3 and R1–E2–E4–R3); the length of the sides is  $S = D/\sqrt{2}$ , where  $D$  (m) is the diagonal length that equals the inner cylinder diameter. The remaining four faces of the cuboid are four rectangles, the smallest sides of which are  $S$  and the longest sides are chosen equal to  $D$ .

Transducers (E1, R1, E2, and R2) are located along the diagonals of the two orthogonal square sections (E1–E4–R1–R4 and E2–E3–R2–R3) of this cuboid and the same distance path  $L$  (m) is given for the upwind channel L1 and for the downwind channel L2.

By neglecting the boundary layer shear near the inner cylinder wall, transit times  $t_1$  of the sound pulse may be calculated, according to

$$t_1 = \frac{L \sin\beta}{V \sin\alpha_1} = \frac{L}{c\sqrt{2}} \frac{1}{\sin\alpha_1} = \frac{L}{c} \frac{1}{\sin\beta + \cos\beta};$$

and, the same for  $t_2$ :

$$t_2 = \frac{L \sin\beta}{V \sin\alpha_2} = \frac{L}{c\sqrt{2}} \frac{1}{\cos\alpha_1} = \frac{L}{c} \frac{1}{\sin\beta - \cos\beta}.$$

Combining these expressions, the sound velocity  $c$  may be obtained by

$$c = \frac{L}{\sqrt{2}} \left( \frac{1}{t_1} + \frac{1}{t_2} \right)^{1/2},$$

and the relative wind speed by

$$V = \frac{L}{\sqrt{2}} \left( \frac{1}{t_1} - \frac{1}{t_2} \right).$$

Then the temperature  $T$  of the dry air may also be calculated using the following expression:

$$T = \frac{c^2}{\gamma_a R_a} \Rightarrow T = \frac{L^2}{2\gamma_a R_a} \left( \frac{1}{t_1} + \frac{1}{t_2} \right).$$

*c. Theoretical times of transit*

From these three last equations, it is easy to calculate the two theoretical transit times  $t_1$  and  $t_2$ :

$$t_{1,2} = \frac{L}{\sqrt{2}(c^2 - V_i^2)^{1/2}} [(2c^2 - V_i^2)^{1/2} \pm V_i].$$

Or, the same times may be written with thermodynamics and geometrics parameters using also the coefficient  $\mu$ . In this case,  $V_o$  and  $T_o$  are the only variables:

$$t_{1,2} = \frac{\sqrt{2}L}{2\gamma RT_o + (\gamma - \gamma\mu^2 - \mu^2 - 1)V_o^2} \times \{ [2\gamma RT_o + (\gamma - \gamma\mu^2 - 1)V_o^2]^{1/2} \pm \mu V_o \}.$$

Then,

$$t_{1,2} = \frac{0.30}{803.74T_o + 0.09V_o^2} \times [(803.74T_o + 0.22V_o^2)^{1/2} \pm 0.36V_o].$$

The resolution of the measurements of velocity and temperature may be calculated from these equations. For

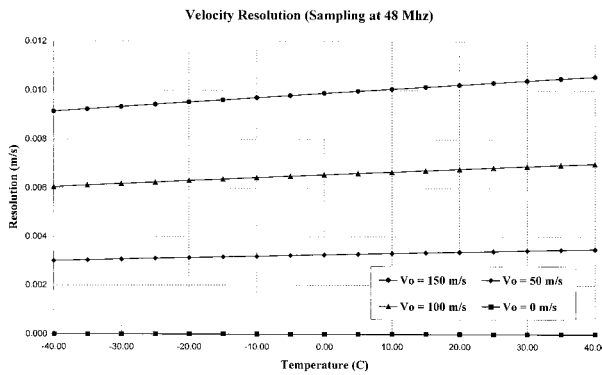


FIG. A2. Theoretical resolution of the AUSAT measurement of velocity with a signal sampled at 48 MHz.

example, with a clock at 48 MHz, a velocity of 100 m s<sup>-1</sup> and a temperature between -40 and +40°C, the velocity resolution is in the range of 0.006–0.007 m s<sup>-1</sup> (Fig. A2) and the temperature resolution is in the range of 0.014°–0.023°C (Fig. A3).

In a future version of the AUSAT, the clock would be adjusted to reach 100 MHz and the theoretical resolutions would be better than 0.004 m s<sup>-1</sup> and 0.012°C.

## APPENDIX B

### The AUSAT is a Natural Frequency Filter

This sensor is essentially designed for the study of fast air temperature fluctuations. So we have to distinguish between its ability to sketch low temperature variation, static behavior, and its performances in presence of very fast fluctuations.

#### a. Static behavior and temporal response to a temperature step

Suppose that a brutal increase in temperature  $\Delta T$  is experienced by the sensor. As it gives the mean temperature in the measuring channel, its temporal response will be a linear increase of temperature.

For an airspeed  $V_o = 100$  m s<sup>-1</sup> thus  $V_i = 40$  m s<sup>-1</sup> and the response time is

$$\tau = d/V_i = 0.15/40 = 3 \text{ ms.}$$

#### b. Response to a periodic variation

For a periodic and stationary temperature field of spatial wavelength  $\lambda$ , the sensor's response is a function of the time with the period  $\tau = \lambda/v$ , the frequency  $f = 1/\tau = v/\lambda$  and the angular frequency  $\omega = 2\pi f = 2\pi v/\lambda$ .

For a linear system, the transfer function  $\theta(f)$  is given by the Fourier transform of the response to a step. Assuming, by simplifying, that for small amplitudes of  $\Delta T$  this theorem may be applied for the AUSAT and by taking into account that the derivative of the temporal

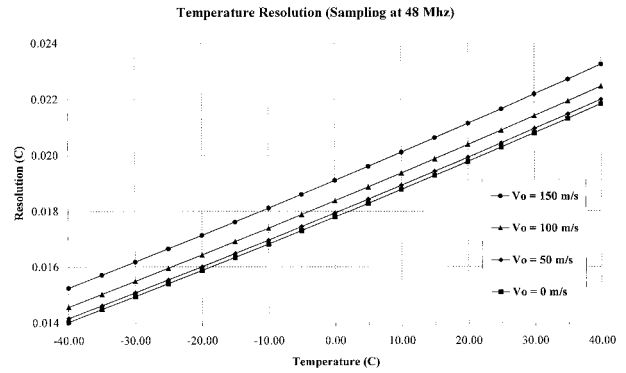


FIG. A3. Theoretical resolution of the AUSAT measurement of temperature with a signal sampled at 48 MHz.

response to the considered step  $\Delta T$  is  $v\Delta T/d$ , so  $\theta(f)$  may be written

$$\theta(f) = \int_{t=0}^{t=d/v} \frac{\Delta T}{d} \exp(-j2\pi ft) dt,$$

and after integration,

$$\theta(f) = \Delta T \frac{\sin\left(\pi f \frac{d}{v}\right)}{\pi f \frac{d}{v}} \exp\left(-j\pi f \frac{d}{v}\right).$$

The amplitude of this expression has the form  $(\sin u)/u$ . The attenuation of spectral components versus time shows that amplitude is equal to zero for multiples of  $V/d$ . For an airspeed  $V_o = 100$  m s<sup>-1</sup>, thus  $V_i = 40$  m s<sup>-1</sup> and the first zero corresponds to  $40/0.15 = 300$  Hz, giving 150 Hz of theoretical bandpass at 3 dB.

## REFERENCES

- Brown, E. N., C. A. Friehe, and D. H. Lenschow, 1983: The use of pressure fluctuations on the nose of an aircraft for measuring air motion. *J. Climate Appl. Meteor.*, **22**, 171–180.
- Etkin, B., 1972: *Dynamics of Atmospheric Flight*. John Wiley and Sons, 579 pp.
- Harmer, J., C. G. Kilsby, S. R. Rudman, and J. H. Seymour, 1990: Temperature measurements on the C130, Met Office Working Group Rep., 44 pp. [Available from The Met. Office, Meteorological Research Flight, Bldg. Y46, Farnborough GU-14-OLX, United Kingdom.]
- Harris, C., 1971: Effects of humidity on the velocity of sound in air. *J. Acoust. Soc. Amer.*, **49**, 890–893.
- Hartman, J., J. Hacher, and H. Kraus, 1990: Correction of data from a salt-spray contaminated temperature sensor, *Bound.-Layer Meteor.*, **50**, 153–169.
- Heymsfield, A. J., J. E. Dye, and C. Biter, 1979: Overestimates of entrainment from wetting of aircraft temperature sensors in cloud. *J. Appl. Meteor.*, **18**, 92–95.
- Khelif, D., S. P. Burns, and C. A. Friehe, 1999: Improved wind measurements on research aircraft. *J. Atmos. Oceanic Technol.*, **16**, 860–875.
- Kinsler, L., 1982: *Fundamentals of Acoustics*. John Wiley and Sons, 480 pp.

- Knudsen, O., 1948: The attenuation of audible sound in fog and smoke. *J. Acoust. Soc. Amer.*, **20**, 849–857.
- Lawson, R. P., 1988: The measurement of temperature from an aircraft in cloud. Ph.D. thesis, University of Wyoming, 336 pp.
- Lenschow, D. H., 1986: *Probing the atmospheric boundary layer*. Amer. Meteor. Soc. 269 pp.
- , and W. T. Pennel, 1974: On the measurement of in cloud and wet bulb temperature from an aircraft. *Mon. Wea. Rev.*, **102**, 447–454.
- Marillier, A., M. Cabane, and D. Cruette, 1991: Preliminary tests of an ultrasonic thermo anemometer for aircraft measurements. *J. Atmos. Oceanic Technol.*, **8**, 597–605.
- Mitsuta, Y., 1966: Sonic anemometer–thermometer for general use. *J. Meteor. Res. Japan*, **44**, 12–23.
- Morera, M., 1995: Essai sur l'influence des différents paramètres intervenant dans le calcul de la vitesse propre du Merlin-IV. *Note de Centre*, 15 pp. [Available from Météo France/CNRM/CAM, Aérodrome du CEV, Bâtiment AMOR, F-91228 Brétigny-sur-Orge, France.]
- Morse, P. M., and K. U. Ingard, 1986: *Theoretical Acoustics*. Princeton University Press, 927 pp.
- Nacass, P. L., 1992: Theoretical errors on airborne measurements of static pressure, impact temperature, air flow angle and air flow speed. NCAR Tech. Note 385, 62 pp. [Available from NCAR, P.O. Box 3000, Boulder, CO 80307.]
- Ovarlez, J., H. C. Cabrita, D. Cadet, and H. Ovarlez, 1978: A balloon-borne sonic anemometer–thermometer. *Fourth Symp. on Meteorological Observations and Instrumentations*, Denver, CO, Amer. Meteor. Soc., 65–68.
- Pruppacher, H. R., and J. D. Klett, 1980: *Microphysics of clouds and precipitation*. D. Reidel, 714 pp.
- Rosemount Engineering Company, 1965: A general technical bulletin on total temperature sensors. Tech. Rep. 7637 32 pp. [Available from Rosemount Engineering Company, P.O. Box 35129, Minneapolis, MN 55435.]
- Smith, S. A., and P. Jonas, 1995: Observations of turbulent fluxes in fields of cumulus clouds. *Quart. J. Roy. Soc.*, **121**, 1185–1208.
- Stickney, T. M., M. W. Shedlov, D. I. Thompson, and F. T. Yakos, 1981: Rosemount total temperature sensors. Tech. Rep. 5755, 28 pp. [Available from Rosemount Engineering Company, P.O. Box 35129, Minneapolis, MN 55435.]
- Suomi, V. E., and J. A. Businger, 1959: Principle of the sonic anemometer–thermometer. Geophys. Res. Paper No. 59, AFCRC-TR-58-235, 673 pp.
- Villain, J., M. Zephoris, and F. Henaff, 1996: Sonde de mesure rapide de la température. Atelier "Expérimentation et Instrumentation." Paper I-b7, 111–115. [Available from Météo France/CNRM, 42 Avenue G. Coriolis, F-31057, Toulouse, France.]